Journal of Alloys and Compounds 571 (2013) 138–144

Contents lists available at SciVerse ScienceDirect

Journal of Alloys and Compounds

journal homepage: www.elsevier.com/locate/jalcom

Dielectric properties, impedance analysis and modulus behavior of $CaTiO_3$ ceramic prepared by solid state reaction

Y.J. Wong [a,*], J. Hassan [a,b], M. Hashim [a,b]

[a] Department of Physics, Faculty of Science, Universiti Putra Malaysia, 43400 Serdang, Selangor, Malaysia
[b] Advanced Materials and Nanotechnology Laboratory, Institute of Advanced Technology (ITMA), Universiti Putra Malaysia, 43400 Serdang, Selangor, Malaysia

ARTICLE INFO

Article history:
Received 10 December 2012
Received in revised form 10 March 2013
Accepted 12 March 2013
Available online 26 March 2013

Keywords:
Dielectric response
Ceramics
Solid state reaction
Sintering

ABSTRACT

Calcium titanate ($CaTiO_3$) with the general formula for perovskites, ABO_3, is of technological importance, particularly with regard to dielectric properties. In this work, $CaTiO_3$ ceramic material was prepared by the conventional solid state reaction method. The dielectric properties, impedance characteristics and modulus behavior of the $CaTiO_3$ ceramic material sintered at 1240 °C were investigated in the frequency range of 10^{-2}–10^6 Hz and temperature range of 100–250 °C. The XRD analysis of the sintered $CaTiO_3$ shows that it is an orthorhombic structure with lattice parameters $a = 5.4398$ Å, $b = 7.6417$ Å, and $c = 5.3830$ Å. The FESEM micrograph shows a significant difference in grain size distribution ranging from 0.26 to 2.32 μm. The AC conductivity, σ_{AC}, is found to increase with increasing temperature within the frequency range of 10^{-2}–10^6 Hz confirming the hopping of electrons to be the conduction mechanism. Due to the decreasing values of the frequency exponent s with increasing temperature, the results of the σ_{AC} are discussed using the correlated barrier height (CBH) model. For dielectric studies, the dielectric constant, ε' is found to decrease with increasing frequency. In the whole temperature range of 100–250 °C, high and low frequency plateau are observed. Each converges at high frequency (>10^5 Hz) for all the temperatures. The frequency dependence of loss tangent, $\tan\delta$, decreases with rise in temperature, with the loss tangent peak shifting to higher frequency. Due to its dielectric characteristics, it is a suitable candidate for developing a variety of capacitors. For the master modulus plot, the shapes remain unchanged in the temperature range considered. The Cole–Cole plots reveal that two primary relaxation processes exist in the sample for each temperature. The Nyquist plots reveal that at temperatures below 150 °C, a linear response in the imaginary part of the impedance, Z'', is noticed. At and above 175 °C, the linear response gradually changes to a semicircle arc. The modulus behavior indicates the presence of correlation between the motions of mobile charge carriers. The plots of Arrhenius diagram of relaxation times of loss tangent, $\tau_{\tan\delta}$, and imaginary part of dielectric modulus, $\tau_{M''}$, obey the Arrhenius law, where the activation energies calculated from the slopes are 2.09 and 2.38 eV respectively.

1. Introduction

Since the discovery of ferroelectricity in barium titanate ($BaTiO_3$) in 1945 [1], a large number of titanate materials, whether pure or doped, have been examined for a wide variety of technological applications. Among the titanate materials, calcium titanate with its chemical formula, $CaTiO_3$, has been extensively investigated due to its many interesting electric and dielectric properties. Consequently, $CaTiO_3$ has gone into various potential technological applications in a wide frequency range spanning microwave to radio frequencies [2]. The demands for $CaTiO_3$ in electronic devices include varistors, capacitors, thermally sensitive resistor element, electrodes, etc. $CaTiO_3$ undergoes phase transition and exhibits different structures, depending on the transition temperature [3]. It displays an orthorhombic structure at room temperature. With the temperature increases to about 1227 °C, a phase transition from the orthorhombic to tetragonal structure occurs [3]. The titanate transforms to the ideal cubic perovskite structure at a higher temperature of about 1327 °C [4–6].

There are a number of processing techniques reported during the past decades for synthesizing $CaTiO_3$, such as sol–gel [7], co-precipitation [7], combustion [8], polymeric precursor [9], and organic–inorganic [10] techniques. A typical preparation route for $CaTiO_3$ involves solid state sintering in which CaO (or $CaCO_3$), and TiO_2 (rutile/anatase) serve as the starting materials with the sintering process performed at about 1377 °C [11]. The solid state method has received a lot of attention due to the low cost and simplicity of the process. However, to have a good understanding of the dielectric behaviors of the material, the dielectric properties can be interpreted in terms of the complex dielectric permittivity, ε_r^*, complex

---

* Corresponding author. Tel.: +60 3 8946 6658; fax: +60 3 8943 5380.
E-mail addresses: yjeng_86@hotmail.com (Y.J. Wong), jumiah@science.upm.edu.my (J. Hassan), mansor@science.upm.edu.my (M. Hashim).

0925-8388/$ - see front matter © 2013 Elsevier B.V. All rights reserved.
http://dx.doi.org/10.1016/j.jallcom.2013.03.123

conductivity, σ^*, complex dielectric modulus, M^*, loss tangent, tan δ, complex impedance, Z^*, and other related physical properties.

There have been few papers which report on studies of the physical properties of $CaTiO_3$. Balachandran and Eror [12] prepared $CaTiO_3$ with different Ca:Ti ratios of 1.003, 1.005, and 1.008 by a liquid mix technique [13,14] and investigated the electrical conductivity of the sample at 1050 and 1100 °C under thermodynamic equilibrium conditions with the oxygen partial pressures, P_{O_2}, in the range of 10^{0}–10^{-19} atm. They concluded that the measured electrical conductivity was exactly the same as those obtained previously in a sample with the ideal Ca:Ti ratio of 1.000. The report also indicated that no obvious changes were found in the absolute values of the conductivity as the Ca:Ti ratio was changed in all the three regions (region 1, $P_{O_2} = 10^{-19}$–10^{-14} atm; region 2, $P_{O_2} = 10^{-13}$–10^{-8} atm; region 3, $P_{O_2} > 10^{-4}$ atm). Recently, Sindhu et .al. [15] studied the rietveld refinement and impedance spectroscopy of $CaTiO_3$. The refinement revealed that $CaTiO_3$ crystallized in orthorhombic symmetry with the *Pbnm* space group at room temperature. In the framework of conductivity, the Nyquist plot revealed a non Debye relaxation behavior with distributed relaxation times. The value of the frequency exponent *s* can be explained with the aid of the correlated barrier hopping (CBH) model. This paper also reported on the dielectric response of materials to an applied electric field in terms of frequency and temperature. The doping of $CaTiO_3$ with different impurities to investigate the electrical properties has been reported in several literatures. One of the literature reported that the electrical conductivity was improved by doping with iron (Fe) and enabled this compound to be an attractive use as a membrane for hydrogen production.

In the present work, $CaTiO_3$ ceramic materials are prepared by the conventional solid state reaction method. The purpose of the present work is to investigate the effect of frequency and temperature on the AC conductivity and dielectric properties of the $CaTiO_3$ ceramic materials within the frequency range 10^{-2}–10^{6} Hz at various temperatures within 100–250 °C. The modulus behavior of the $CaTiO_3$ is also investigated since no reported studies have been found to utilize this mode of analysis on the titanate.

2. Experimental

The $CaTiO_3$ ceramic samples were synthesized using the conventional solid state sintering method. High purity of CaO (99.95% purity, Alfa Aesar) and anatase–TiO_2 (99.99% purity, Alfa Aesar) were used as starting powders. They were mixed together according to their molecular weight ratio by ball milling for 24 h using ceramic balls. The milled powders were then placed in a ceramic boat and were pre-sintered at 1100 °C for 10 h in air using an electric furnace. The calcined products were crushed and ground using a mortar and pestle, followed by sieving using a 45 μm test sieve to obtain better powder homogeneity. The sieved powders were compacted into disk-shaped samples (pellets) with a 20 mm diameter under a pressure of 50 kPa. The compacted pellets were subsequently sintered at 1240 °C for 10 h in air.

The formation of the crystalline phase of the sintered samples was analyzed by X-ray diffractometry (XRD) at room temperature using a PANalytical X'Pert Pro diffractometer system with Cu Kα radiation from 20° to 80° at 2θ intervals. The microstructure and grain size distribution of the sintered samples were examined by Field Emission Scanning Electron Microscopy (FESEM) using a FEI 230 Nova NanoSEM machine. Grain sizes on micrographs were determined using a built in cursor. For dielectric measurement, both surfaces of the sintered pellets were polished using a fine abrasive paper to make them parallel. After the polishing, silver conductive paint was deposited on both surfaces of the sintered pellets. The dielectric properties of the sintered pellets in terms of complex dielectric permittivity, ε^*, complex dielectric modulus, M^*, and complex impedance, Z^*, were measured in the frequency range 10^{-2}–10^{6} Hz and in the temperature range 100–250 °C using a High Resolution Dielectric Analyzer.

3. Results and discussion

3.1. X-ray structural and microstructural analysis

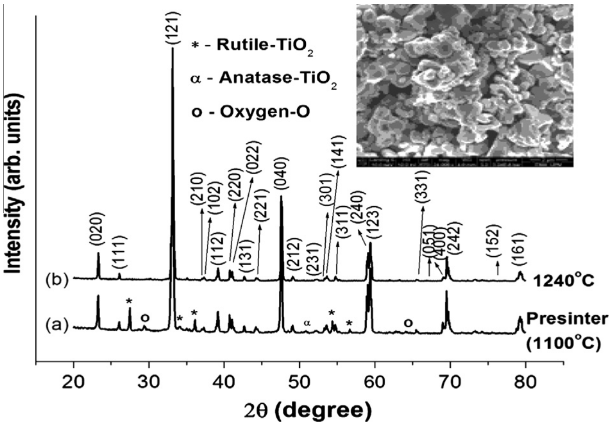

Fig. 1. X-ray diffraction (XRD) patterns of $CaTiO_3$ calcined at: (a) 1100 °C and sintered at and (b) 1240 °C. The FE-SEM micrograph of $CaTiO_3$ sintered at 1240 °C (inset).

Table 1
Comparison of observed and calculated *d*-values, peak position in 2θ for the miller indices (*hkl*) of all the XRD peaks corresponding to $CaTiO_3$ sintered at 1240 °C.

h	*k*	*l*	$2\theta_{obs}$	$2\theta_{cal}$	d_{obs} (Å)	d_{cal} (Å)	Relative intensity (%)
0	2	0	23.3188	23.3003	3.81476	3.81458	14.68
1	1	1	26.1097	26.0878	3.41298	3.41297	3.14
1	2	1	33.1991	33.1746	2.6986	2.6983	100
2	1	0	35.0755	35.0755	2.55841	2.55841	1.1
1	0	2	37.3466	37.3466	2.40789	2.40789	1.9
1	1	2	39.1917	39.163	2.29867	2.29839	4.8
2	2	0	40.7639	40.7486	2.21358	2.21254	4.9
0	2	2	41.0606	41.0498	2.19826	2.197	3.6
1	3	1	42.6948	42.6717	2.11783	2.11717	1.9
2	2	1	44.3166	44.2902	2.04402	2.04349	1.3
0	4	0	47.5959	47.5752	1.91056	1.90977	34.2
2	1	2	49.1074	49.0773	1.85524	1.85477	2.1
2	3	1	52.3125	52.2361	1.74887	1.7498	0.2
3	0	1	53.3443	53.3291	1.71603	1.71648	1.8
1	4	1	53.617	53.6175	1.70936	1.70793	2.2
3	1	1	54.7763	54.7671	1.67589	1.67476	3.2
2	4	0	59.1021	59.1102	1.56184	1.56165	9
1	2	3	59.3897	59.392	1.55625	1.55491	24
0	5	1	63.2111	63.2136	1.47106	1.46979	0.5
3	3	1	65.5706	65.5312	1.42357	1.42331	1.1
4	0	0	69.071	69.071	1.35988	1.35988	3.6
2	4	2	69.5423	69.5452	1.35181	1.35064	14.5
1	5	2	73.2736	73.2736	1.29191	1.29191	1
1	6	1	79.159	79.159	1.20989	1.20898	5.4

Fig. 1 depicts the XRD patterns of the $CaTiO_3$ samples calcined at 1100 °C and subsequently sintered at 1240 °C for 20 h at room temperature in air atmosphere. The $CaTiO_3$ phase is confirmed by comparing the observed XRD patterns with the respective Inorganic Crystal Structure Database (ICSD) pattern [16]. Immediately after the 1100 °C calcination, most of the sharp XRD peaks are identified as belonging to the orthorhombic-type $CaTiO_3$ phase in agreement with the ICSD No. 98-007-7005. The remaining of the small XRD peaks are ICSD-traced to be residual rutile, anatase and oxygen. After further annealing at 1240 °C, all the XRD peaks are completely ICSD-matched, thus confirmed to be those of a single-phase $CaTiO_3$-type orthorhombic (*Pnma*) structure. After a rietveld refinement of the single-phase XRD profile, the refined lattice parameters of the $CaTiO_3$ are found to be in close agreement with the literature data for $CaTiO_3$ [16]. Further crystallographic details are given in Table 1.

A FE-SEM micrograph of the sintered $CaTiO_3$ pellet is shown in Fig. 1 (inset). The morphology reveals some residual pores among micron-sized loosely connected grains, suggesting that further densification is possible. The microstructure shows a non-uniform

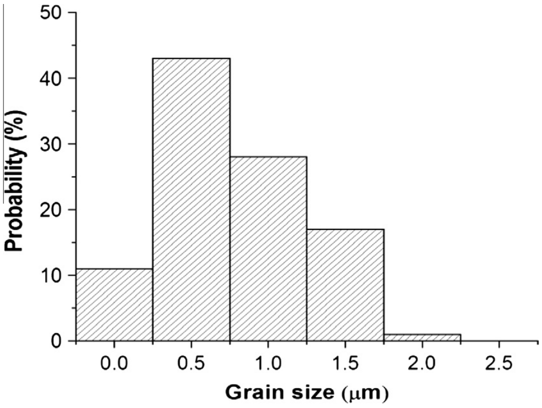

Fig. 2. Histogram of grain size distribution of $CaTiO_3$ sintered at 1240 °C.

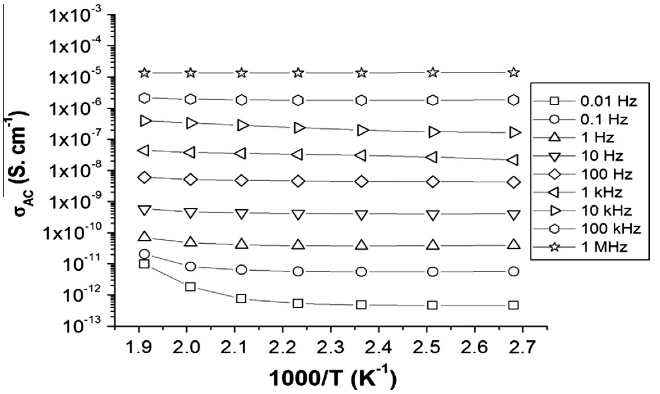

Fig. 3. Variation of AC conductivity, σ_{AC} as a function of reciprocal temperature (1000/T) at different selected frequencies for $CaTiO_3$ sintered at 1240 °C.

distribution of grain sizes as evidenced by the 0.26–2.32 μm grain-size range in Fig. 2. However, most of the grains are in the 0.5–1.0 μm range.

3.2. Frequency and temperature dependence of AC conductivity

Fig. 3 shows plots of the AC conductivity, σ_{AC}, as a function of reciprocal sample temperature (1000/T) at selected frequencies for the $CaTiO_3$ sintered at 1240 °C. As seen in Fig. 3, σ_{AC} continuously increases with increasing temperature within the frequency range of 10^{-2}–10^4 Hz. For σ_{AC} at the higher frequencies of 10^5 Hz and 10^6 Hz, σ_{AC} shows a temperature independent behavior in the considered range of temperatures. The boosting of σ_{AC} with rising temperature indicates that σ_{AC} which originates from different localized states in the gap [17] is a thermally activated process. Specifically, the temperature-dependent σ_{AC} exhibits different rates of increase, in which σ_{AC} increases at a very gradual rate at the lower temperatures, and then at a fast rate at the higher temperatures. A possible explanation of this behavior is the hopping of electrons between the localized states is induced by the applied electric field frequency, particularly in the low temperature region and is induced by the applied electric field frequency in addition to being excited by the energy in the high temperature region [18]. With increasing frequency, σ_{AC} increases strongly indicating the hopping of electrons to be a conduction mechanism [19].

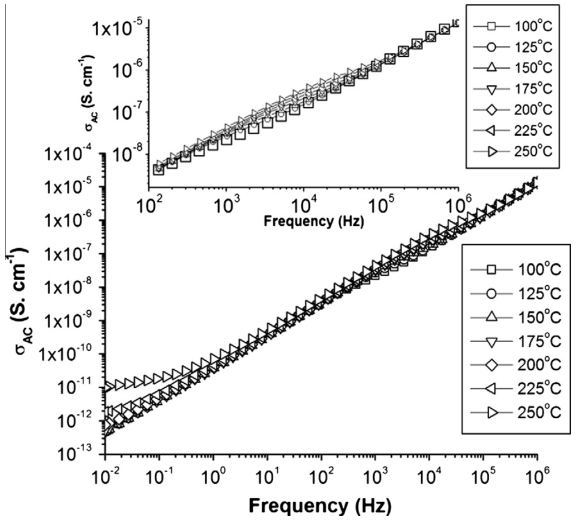

Fig. 4. Variation of AC conductivity, σ_{AC} as a function of frequency at various temperatures for $CaTiO_3$ sintered at 1240 °C.

Fig. 4 shows plots of the AC conductivity, σ_{AC}, as a function of frequency in the frequency range of 10^{-2}–10^6 Hz at various sample temperatures in the range of 100–250 °C for the $CaTiO_3$ sintered at 1240 °C. It is obvious that σ_{AC} increases as the frequency is increased, with σ_{AC} exhibits similar curve shapes with increasing values of σ_{AC} and with elevated temperature in the frequency range of 10^3 – 10^5 Hz (inset). At the higher frequencies above 10^5 Hz, σ_{AC} at different temperatures begins to merge into a single frequency-dependent linear plot with almost the same values of σ_{AC} at a given frequency. That σ_{AC} increases linearly with increasing frequency could be due to active motion of electrons, atoms, and hopping between the equilibrium sites [20]. σ_{AC} is seen to obey the universal power law behavior, or called Jonscher's law [21] according to the following relation:

$$\sigma_{AC} = A\omega^s = \sigma_{total} - \sigma_{DC}, \quad 0 < s < 1 \qquad (1)$$

where A is a constant which is poorly dependent on temperature, ω is an angular frequency ($\omega = 2\pi f$), s is a frequency exponent, σ_{total} is the total measured conductivity, and σ_{DC} is the direct current (DC) conductivity. The low values of σ_{AC} in a relatively low frequency region could be attributed to the blocking of ions between the electrode and samples [22].

The frequency exponent s varies in the range 0–1. It is temperature dependent which outlines many body interactions of the electrons, impurities and charges, besides being useful for distinguishing which type of AC conduction mechanism is involved in the investigated sample [23,24]. The values of s are determined from the slope of the linear σ_{AC} versus frequency curve (Fig. 4). The s values obtained are in the range of 0.792–0.957, in which the values of s decrease with the rise in temperature, as shown in Fig. 5a. Various theoretical models such as the quantum-mechanical tunneling (QMT) model, the correlated barrier hopping (CBH) model, the small polaron tunneling model, and the overlapping large polaron tunneling (OLPT) model have been developed in order to investigate the AC conduction mechanism in dielectric samples. Among these models, the CBH model, proposed by Elliott [25], is the most appropriate model. In this model, the charge carriers hop between two sites over a barrier separating them, and the frequency exponent s decreases continuously with increasing temperature [26], which is in good agreement with the results obtained here. The frequency exponent s in the CBH model can be expressed in relation [27] as shown below:

$$S = 1 - \{6kT/[W_M - kT\ln(1/\omega\tau_0)]\} \qquad (2)$$

where W_M is the maximum barrier height, k is the Boltzmann constant, T is the absolute temperature, ω is the angular frequency, and τ_0 is the characteristic relaxation time. The value of W_M can be

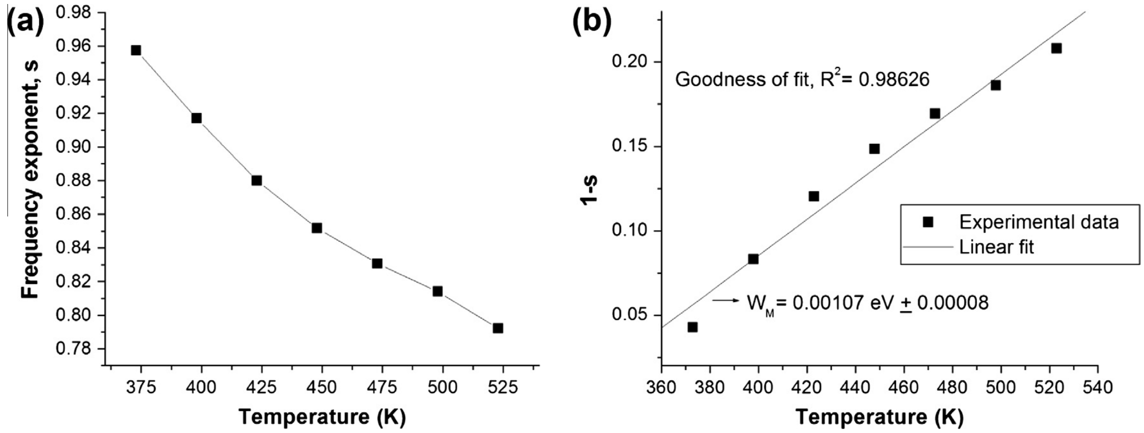

Fig. 5. Temperature dependence of: (a) the frequency exponent *s* and (b) *1-s* for $CaTiO_3$ sintered at 1240 °C.

calculated from the slope of 1-*s* versus *T* curve plotted, as shown in Fig. 5b.

3.3. Frequency dependence of dielectric constant and loss tangent

The effect of frequency on the dielectric constant, ε', and the loss tangent, $\tan\delta$, at various temperatures are studied for the $CaTiO_3$ sintered at 1240 °C, as depicted in Fig. 6. Generally, ε' and $\tan\delta$ exhibit the same pattern in the whole frequency range for all the temperatures. A continuous decreasing trend in ε' with increasing frequency is seen as illustrated in Fig. 6a. Two plateaus are observed with one occurring in the lower frequency region (10^0–10^3 Hz) and another in the higher frequency region (10^4–10^6 Hz) for all the measured temperatures. It is worth noticing that the lower frequency plateau shifts to the higher frequency region with increasing temperature. Each lower frequency plateau exhibits a steep decrease afterward and converges at the same level for all temperatures (i.e. high frequency plateau). Alternatively, ε' is found to be almost independent of frequency in the high frequency region above 10^5 Hz for all the temperatures. The variation of ε' with frequency can be discussed on the principle of Maxwell–Wagner type interfacial (space charge) polarization in which under the influence of an applied external electric field, the space charge polarization is produced due to the contribution of grain and grain boundaries of a dielectric, which produces the localized accumulation of space charge [28]. The reduction of ε' along the whole frequencies for all the temperatures can be explained by the space charge carriers are no longer to be able to line up their axes parallel to an applied external electric field, as the change in the direction of the electric field become rapid and the alternation of the space charge carriers' direction lags behind that of the electric field when the frequency is further increased [28]. As the temperature is raised, the dipoles acquire adequate thermal energy to follow the change in the electric field, thus ε' is found to increase with increasing temperature within the frequency range 10^{-2}–10^5 Hz. Beyond the frequency of 10^5 Hz, ε' is no longer follow the changes of temperature and it keeps almost constant along this frequency region.

In Fig. 6b, $\tan\delta$ is obviously dependent on the temperature in which $\tan\delta$ shows an increase with increasing temperature. $\tan\delta$ is found to decrease in the frequency range 10^{-2}–10^2 Hz at different temperatures (150–250 °C), except for the temperatures of 100 and 125 °C, where a small $\tan\delta$ peak is observed in the lower frequency range of 10^{-1}–10^0 Hz. The small $\tan\delta$ peak at the low temperatures and frequency indicates that the possibility of the dipole polarization. Beyond the frequency of 10^2 Hz, $\tan\delta$ increases, passes through a maximum value, and then decreases for all the temperatures. The decreasing trends of $\tan\delta$ right after the occurrence of the peaks show that this sample exhibits almost zero dielectric loss at higher frequencies. This suggests that the $CaTiO_3$ sample is a lossless material at higher frequencies. The high value of $\tan\delta$ at the lower frequency could be due to the free charge motion in the sample and is associated with the conductivity relaxation [29]. The amplitude of $\tan\delta$ peak increases with the shifting of the broad $\tan\delta$ peak towards the higher frequency with elevated temperature.

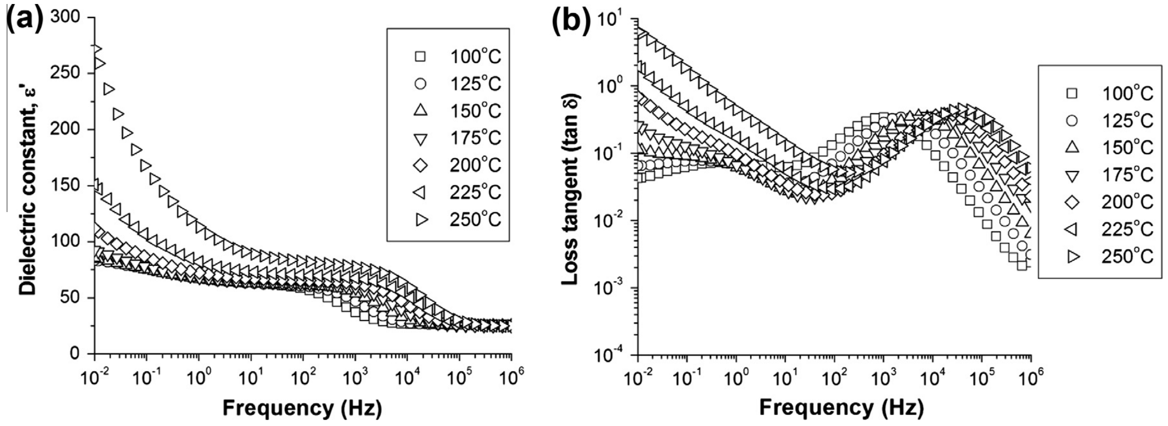

Fig. 6. Variation of: (a) ε' and (b) $\tan\delta$ of $CaTiO_3$ sintered at 1240 °C as a function of frequency at various temperatures.

Based on the investigation of ε' and $\tan\delta$ along the frequency range 10^{-2}–10^{6} Hz between 100 and 250 °C, $CaTiO_3$ could be a potential candidate ceramic material for manufacturing capacitors. In practice, due to its temperature and frequency dependence characteristic of ε' within the frequency range 10^{-2}–10^{5} Hz, it finds applications in capacitors which are used for power supply bypassing and decoupling. Beyond the operating frequency of 10^{-5} Hz, due to the increasing temperature gives ineffective contributions to ε', it could be developed into temperature stable multilayer capacitors which used in resonant circuits and filtering applications.

By taking $BaTiO_3$ sample as a comparative example [30], ε' of pure $BaTiO_3$ bulk sample prepared by solid state method showed a value of about 1000, whereas the obtained ε' of $CaTiO_3$ in our case is comparatively small, which is about 27.4 at room temperature. Despite of the huge difference of ε' between both distinct samples, they can be developed into various type of dielectrics used for passive components regarding to their functionality. Based on the values of ε', $CaTiO_3$ with low ε' value of 27.4 can be used to make Class 1 dielectric capacitors coded C0G, while $BaTiO_3$ with high ε' value of 1000 can be used to produce Class 2 dielectric capacitors coded X5R. The codes of Class 1 and 2 dielectrics are classified by the Electronic Industries Alliance (EIA) [31].

3.4. Cole–Cole and Nyquist plots

The complex Argand plane plots between ε'' and ε', also known as Cole–Cole plots, for the $CaTiO_3$ sintered at 1240 °C at several temperatures are shown in Fig. 7a. A semicircle at the high frequency and an incomplete semicircle at the low frequency are obtained for each temperature indicating that two primary relaxation processes exist in the sample in the mentioned temperature interval. The Cole–Cole plot is known to be described by the empirical relation [32] given as:

$$\varepsilon^* = \varepsilon' - j\varepsilon'' = \varepsilon_\infty + [(\varepsilon_s - \varepsilon_\infty)/1 + (j\omega\tau)^{1-\alpha}] \tag{3}$$

where ε^* is the complex dielectric constant, ε_s and ε_∞ are the low and high frequency values of ε' respectively, $j = \sqrt{(-1)}$, $\omega = 2\pi f$ is the angular frequency, τ is the mean relaxation time, and α is a measure of the distribution of relaxation times, $\tau = \omega^{-1} = 1/2\pi f$. The Cole–Cole plots indicate the polydispersive nature of the dielectric relaxation of the $CaTiO_3$, as the parameter, α, as determined from the angle subtended by the radius of the circle with the real axis passing through the origin of ε'-axis, showing a consistent increase in the interval 0.18–0.39 with increasing temperature.

The complex impedance plots between Z'' and Z', also known as Nyquist plots, for the $CaTiO_3$ sintered at 1240 °C at several temperatures are shown in Fig. 7b. The Nyquist plots reveal that with the change in temperature, distinct effects on the characteristic impedance spectrum are observed. The Nyquist plots reveal that at the temperature below 150 °C, a straight line with large slope is noticed, suggesting the insulating behavior of the sample [33]. The gradient of the slope show a decrease from 100 to 150 °C. At and above 175 °C, the linear response gradually changes to semicircular arc indicating the increase in the conductivity of the sample [34]. The semicircular arcs are visible in the high frequency zone with reduced impedance values as the temperature is increased. As the temperature is further increased above 498 K, other semicircular arcs appear in the low frequency zone. The presence of the low and high frequency semicircular arcs can be interpreted by modeling an equivalent electrical circuit, which comprises two parallel resistive, *R* and capacitive, *C* components connected in series [35], as shown in Fig. 8. The two parallel *R-C* components are characterized by the parallel combination of (R_b–C_b) and (R_{gb},C_{gb}), in which R_b and C_b represent the bulk (grain) resistance and the bulk capacitance, whereas R_{gb} and C_{gb} resemble the grain boundary resistance and the grain boundary capacitance (Fig. 8). Hence, the appearance of low frequency semicircular arc is attributed to the grain boundary effects in the material arising due to the parallel combination of R_{gb} and C_{gb}. The high frequency semicircular arc appears attributed to the bulk property of the material arising due to the parallel combination of R_b and C_b.

3.5. Frequency dependence of real part and imaginary part of dielectric modulus

The complex dielectric modulus analysis is a convenient visual monitor to investigate the electrical transport phenomena in ceramic materials and to distinguish the microscopic processes responsible for localized dielectric relaxation [36]. The complex dielectric modulus, M^*, is given by the inverse of complex dielectric constant and is formulated as follows [37]

$$M^* = 1/\varepsilon^* = j\omega C_0 Z^* = M' + jM'' \tag{4}$$

$$M' = \omega C_0 Z'' = \varepsilon''/(\varepsilon' + \varepsilon'')^2 \tag{5}$$

$$M'' = \omega C_0 Z' = \varepsilon''/(\varepsilon' + \varepsilon'')^2 \tag{6}$$

where M' and M'' are the real and imaginary part of the dielectric modulus respectively, $C_0 = \varepsilon_0 A/d$ is the geometrical capacitance

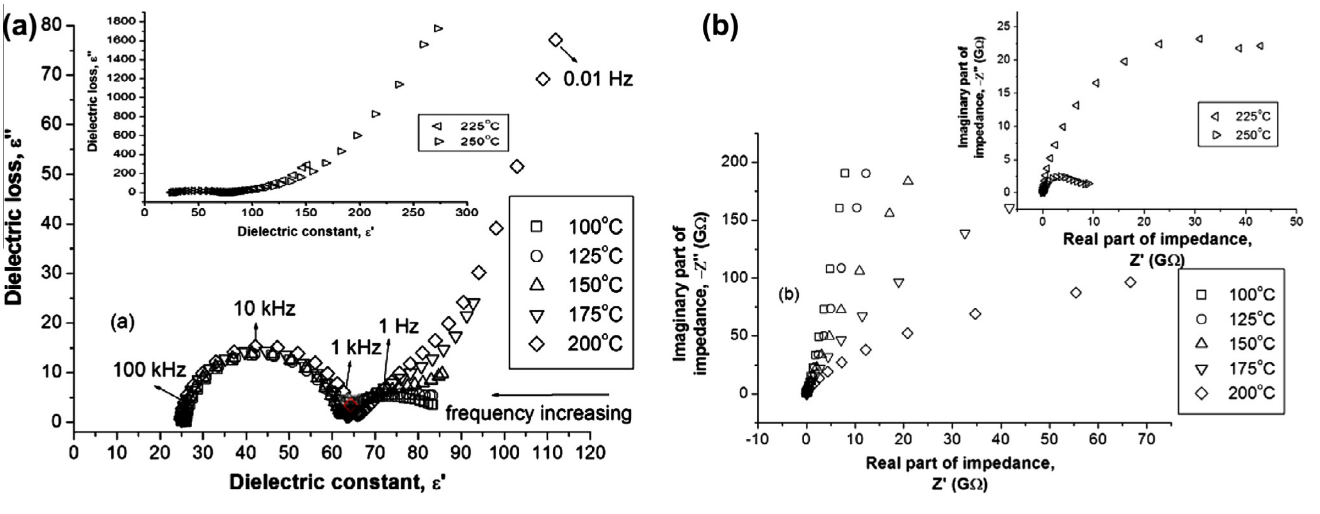

Fig. 7. The plots of: (a) Cole–Cole (ε'' vs ε') and (b) Nyquist (Z'' vs Z').

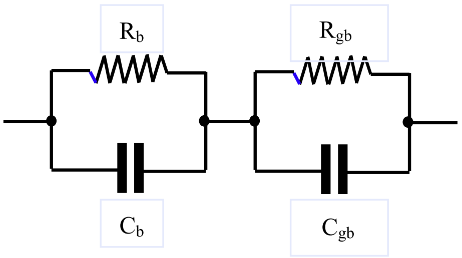

Fig. 8. Equivalent electrical circuit.

(where ε_0 = free space of permittivity = 8.854×10^{-12}, A = area of electrode surface, d = thickness of the specimen).

The graph of the real part of the dielectric modulus, M', as a function of frequency at different temperatures is shown in Fig. 9a. The values of M' approach zero at the low frequencies for most of the temperatures. These observations conclude the electrode polarization makes an almost negligible contribution towards M' [38]. M' shows gradual increase with increasing frequency and reaches almost constant values above 10^5 Hz for all the temperatures. As the temperature is increased, the dispersion region of M' is clearly observed especially within the frequency region 10^3–10^5 Hz and the dispersion shifts to the higher frequency with increasing temperature. It is worth noticing that M' decreases with increasing temperature along the frequency range studied.

The graph of the imaginary part of the dielectric modulus, M'', as a function of frequency at different temperatures is shown in Fig. 9b. With the rise in temperature, the position of the peak of M'' shifts towards the higher frequency and the height of the peak of M'' increases, indicating the presence of dielectric relaxation which is thermally activated, in which the hopping process of charge carriers is predominant. The depressed peak of M'' is also noticed in the lower frequency region at the higher temperatures of 225 and 250 °C. The presence of two peaks of M'' in the temperature indicates that at least two relaxation processes occur in the sample, in which the higher frequency peak can be attributed to the high-frequency dipolar polarization, whereas the lower frequency peak is due to low-frequency dipolar polarization [39]. From the view of the higher frequency peak of M'' for each temperature, the frequency region below the peak represents the range in which the charge carriers are mobiles over long distances [40], whereas the frequency region above the peak determines the range in which the charge carriers are confined to the potential wells being mobile on short distances within the wells [41,42].

3.6. Arrhenius diagram of relaxation time as a function of reciprocal temperature

The scaling behavior of the material is explained by the variation of M''/M''_{max} with log (f/f_{max}) at different temperatures (Fig. 9b inset) and it shows that the shape and FWHM of the asymmetric M''/M''_{max} curve remain constant in the temperature range studied, implying a non-exponential behavior of the conductivity relaxation. Further, the overlapping of the high frequency M''/M''_{max} peaks for all the temperatures into a single master curve indicate that the same relaxation mechanism at various temperatures is described for $CaTiO_3$.

The frequency corresponds to the maximum peaks of M'' and tan δ for a particular temperature is denoted as $f_{max\ M''}$ and $f_{max\tan\delta}$ respectively. The relaxation time of M'', $\tau_{M''}$ and tan δ, $\tau_{\tan\delta}$ has been calculated using the relation [43]:

$$\tau_{M''} = 1/\omega_{max} = 1/2\pi f_{max} M'' \tag{7}$$

$$\tau_{\tan\delta} = 1/\omega_{max} = 1/2\pi f_{max\tan\delta} \tag{8}$$

The plots of Arrhenius diagram of the relaxation times of $\tau_{\tan\delta}$ and $\tau_{M''}$ are shown in Fig. 10. Both plots obey the Arrhenius law, where the activation energy calculated from the slopes is 2.09 and 2.38 eV respectively.

4. Conclusion

$CaTiO_3$ samples were successfully synthesized by the conventional solid state reaction method. The X-ray Diffraction studies confirm the orthorhombic structure of the $CaTiO_3$ samples with the *Pbnm* space group at room temperature. The microstructure of the samples is found to have the grain size distribution ranging from 0.26 to 2.32 μm. The AC conductivity, σ_{AC}, which is found to increase with increasing temperature within the frequency range of 10^{-2}–10^6 Hz strongly indicates the hopping of electrons to be a conduction mechanism. The continuous decrease in the values of the frequency exponent s with increasing temperature can be well-explained using the correlated barrier height (CBH) model,

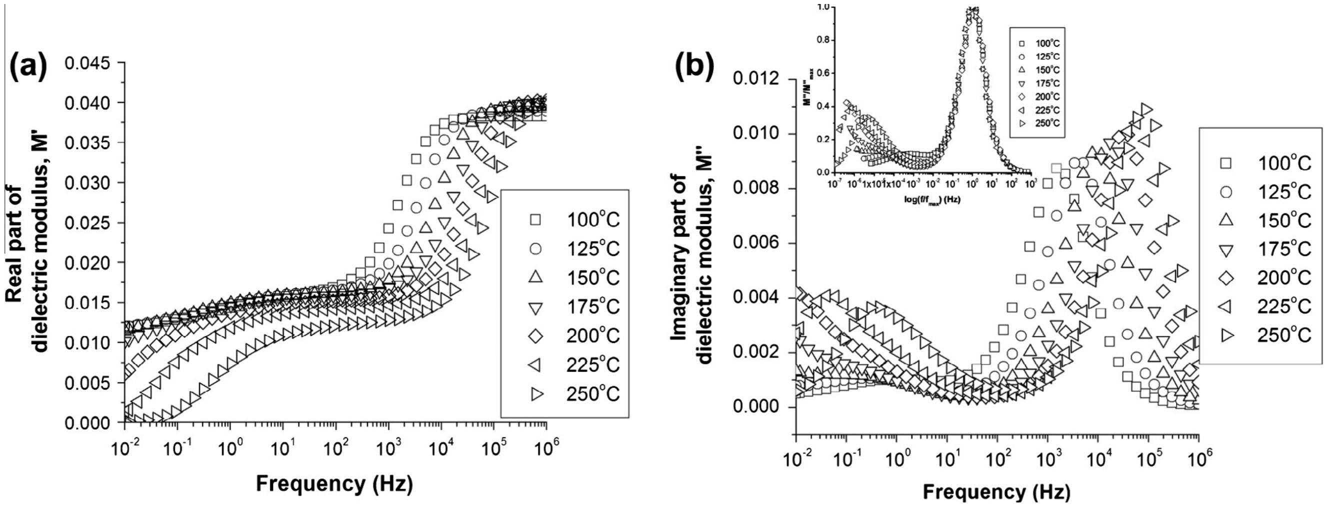

Fig. 9. Frequency dependence of: (a) M' and (b) M'' of $CaTiO_3$ sintered at 1240 °C at different temperatures. Master modulus plot of $CaTiO_3$ sintered at 1240 °C (inset figure 9(b)).

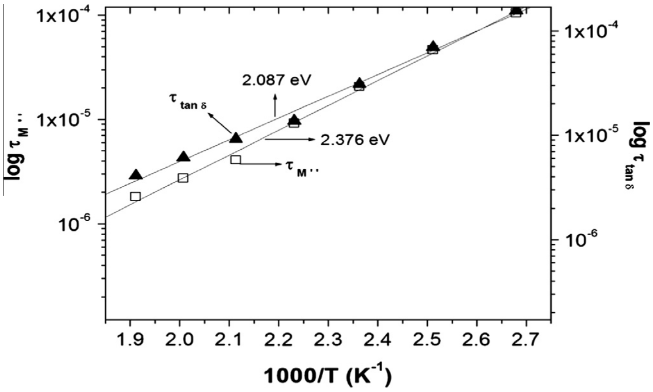

Fig. 10. Arrhenius diagram of relaxation times, $\tau_{M''}$ and $\tau_{\tan\delta}$ as a function of reciprocal temperature 1/T.

suggesting the conduction takes place through the large polaron hopping mechanism. The decreasing trend of the dielectric constant, ε', with increasing frequency is observed for all the temperatures. The variation of ε' with frequency can be discussed on the principle of Maxwell–Wagner type interfacial (space charge) polarization. The Cole–Cole plots reveal two primary relaxation mechanisms in operation for all the temperatures. The values of α increase with increasing temperature, confirming the polydispersive nature of the dielectric relaxation of the $CaTiO_3$. The Nyquist plots reveal that the insulating behavior of the sample at the temperature below 150 °C. At and above 175 °C, the linear response gradually changes to a semicircular arc indicating an increase in conductivity of the sample. The presence of the low and high frequency semicircular arcs at and above 225 °C arise from the contribution of grain-bulk and grain-boundary regions of the sample. The loss tangent ($\tan\delta$) peak and imaginary part of dielectric modulus (M'') peak shift to the higher frequency region with increasing temperature indicating the presence of dielectric relaxation which is thermally activated, in which a hopping process of charge carriers is predominant. The plots of Arrhenius diagram of relaxation times of $\tau_{\tan\delta}$ and τ_M'' obey the Arrhenius law, where the activation energies calculated from the slopes are 2.09 and 2.38 eV respectively.

Acknowledgements

This research was financially supported from the Fundamental Research Grant Scheme (FRGS) Project No.: 01-04-10-862FR. The authors acknowledge the Department of Physics, Faculty of Science UPM and Institute of Advanced Technology (ITMA) UPM.

References

[1] N. Santha, M.T. Sebastian, Mater. Res. Bull. 43 (2008) 2278–2284.
[2] A.M.A.E. Ata, S.M. Attia, T.M. Meaz, Solid State Sci. 6 (2004) 61–69.
[3] Y. Ni, Z. Zhang, D. Wang, Y. Wang, X.B. Ren, J. Alloys Comp. in Press (available online 16 February 2012).
[4] M. Yashima, R. Ali, Solid State Ionics 180 (2009) 120–126.
[5] C.J. Howard, R.L. Withers, B.J. Kennedy, J. Solid State Chem. 160 (2001) 8–12.
[6] T. Matsui, H. Shigematsu, Y. Arita, Y. Hanajiri, N. Nakamitsu, T. Nagasaki, J. Nucl. Mater. 247 (1992) 72–76.
[7] C. Sun, K.N. Sun, Phys. B: Condens. Matter 391 (2007) 335–338.
[8] M. Muthuraman, K.C. Patil, S. Senbagaraman, A.M. Umarji, Mater. Res. Bull. 31 (1996) 1375–1381.
[9] Y. Pan, Q. Su, H. Xu, T. Chen, W. Ge, C. Yang, M. Wu, J. Solid State Chem. 174 (1) (2003) 69–73.
[10] S.J. Lee, Y.C. Kim, J.H. Hwang, J. Ceram. Process. Res. 5 (2004) 223–226.
[11] S. Tamborenea, A.D. Mazzoni, E.F. Aglietti, Thermochim. Acta 411 (2004) 219–224.
[12] U. Balachandran, N.G. Eror, Mater. Sci. Eng. 54 (1982) 221–228.
[13] U. Balachandran, B. Odekirk, N.G. Eror, J. Solid State Chem. 41 (1982) 185–194.
[14] M.P. Pechini, Method of preparing lead and alkaline earth titanates and niobates and coating method using the same to form a capacitor. US Patent No. 3 330 697, 11 July 1967.
[15] M. Sindhu, N. Ahlawat, S. Sanghi, A. Agarwal, R. Dahiya, N. Ahlawat, Curr. Appl. Phys. 12 (2012) 1429–1435.
[16] D. Pandey, A. Chandra, Wroclaw 1 (2002) 1.
[17] A.M. Farid, A.E. Bekheet, Vacuum 59 (2000) 932–939.
[18] L.M.S. El-Deen, Mater. Chem. Phys. 65 (2000) 275–281.
[19] M. Okutan, E. Basaran, H.I. Bakan, F. Yakuphanoglu, Phys. B 364 (2005) 300–305.
[20] A.R. Long, Adv. Phys. 31 (1982) 553–637.
[21] A.K. Jonscher, Nature 267 (1977) 673–679.
[22] C.R. Mariappan, G. Govindaraj, Mater. Sci. Eng. B 94 (2002) 82–88.
[23] A. Mansingh, A.K. Sinha, P.N. Dheer, M. Sayer, Philos. Mag. B 50 (1984) 621–634.
[24] S. Hazra, A. Ghosh, Phys. Rev. B 55 (1997) 6278.
[25] S.R. Elliott, Philos. Magn. 36 (1977) 1291–1304.
[26] T. Winie, A.K. Arof, Ionics 10 (2004) 193–199.
[27] R.I. Mohomed, J. Phys. Chem. Solids 61 (2000) 1357–1361.
[28] M. Chanda, Science of Engineering Materials, vol. 3, The Macmillan Company of India Ltd., New Delhi, 1980. p. 103.
[29] K.S. Rao, D.M. Prasad, P.M. Krishna, B. Tilak, K.C. Varadarajulu, Mater. Sci. Eng. B 133 (2006) 141–150.
[30] V. Paunovic, L. Zivkovic, L. Vracar, V. Mitic, M. Miljkovic, Serbian J. Electron Eng. 1 (3) (2004) 89–98.
[31] R. Mikkenie, Materials development for commercial multilayer ceramic capacitors, Doctor of Philosophy Thesis, University of Twente, The Netherlands.
[32] K.S. Cole, R.H. Cole, J. Chem. Phys. 9 (1941) 341–351.
[33] C.K. Suman, K. Prasad, R.N.P. Choudhary, Mater. Chem. Phys. 97 (2006) 425–430.
[34] K.S. Rao, P.M. Krishna, T.S. Latha, D.M. Prasad, Mater. Sci. Eng. B 131 (2006) 127–134.
[35] E.A. Fattah, I. Saad, J. Optoelectron. Adv. Mater. 7 (2005) 2743–2752.
[36] W.X. Yuan, Solid State Sci. 14 (2012) 330–334.
[37] P.B. Macedo, C.T. Moynihan, R. Bose, J. Phys. Chem. Glass 13 (1972) 171–179.
[38] A.K. Himanshu, B.K. Choudhary, S.N. Singh, D.C. Gupta, S.K. Bandyopadhayay, T.P. Sinha, Solid State Sci. 12 (2010) 1231–1234.
[39] S. Dutta, S. Bhattacharya, D.C. Agrawal, Mater. Sci. Eng. B 100 (2003) 191–198.
[40] D.K. Mahato, A. Dutta, T.P. Sinha, Indian J. Pure Appl. Phys. 49 (2011) 613–618.
[41] K.L. Nagi, C. Leon, Solid State Ionics 125 (1998) 81.
[42] P. Pissis, A. Kyritsis, Solid State Ionics 97 (1997) 105.
[43] M. Ram, S. Chakrabarti, J. Phys. Chem. Solids 69 (2008) 905–912.